



EUROfusion

WPMAT-PR(18) 19224

C Robertson et al.

**Screw dislocation interaction with
irradiation defect loops in α -iron:
investigation of cross-slip effect using
dislocation dynamics simulations**

Preprint of Paper to be submitted for publication in
Modelling and Simulation in Materials Science and
Engineering




This work has been carried out within the framework of the EUROfusion Consortium and has received funding from the Euratom research and training programme 2014-2018 under grant agreement No 633053. The views and opinions expressed herein do not necessarily reflect those of the European Commission.

This document is intended for publication in the open literature. It is made available on the clear understanding that it may not be further circulated and extracts or references may not be published prior to publication of the original when applicable, or without the consent of the Publications Officer, EUROfusion Programme Management Unit, Culham Science Centre, Abingdon, Oxon, OX14 3DB, UK or e-mail Publications.Officer@euro-fusion.org

Enquiries about Copyright and reproduction should be addressed to the Publications Officer, EUROfusion Programme Management Unit, Culham Science Centre, Abingdon, Oxon, OX14 3DB, UK or e-mail Publications.Officer@euro-fusion.org

The contents of this preprint and all other EUROfusion Preprints, Reports and Conference Papers are available to view online free at <http://www.euro-fusionscipub.org>. This site has full search facilities and e-mail alert options. In the JET specific papers the diagrams contained within the PDFs on this site are hyperlinked



Screw dislocation interaction with irradiation defect loops in α -iron: investigation of cross-slip effect using dislocation dynamics simulations

Y. Li*, C. Robertson, M. Shukeir, L. Dupuy

DEN-Service de Recherches Métallurgiques Appliquées, CEA, Université Paris-Saclay, F-91191, Gif-sur-Yvette, France

Abstract

Plastic strain spreading in post-irradiated ferritic materials takes the form of thin, wavy shear bands. Associated plasticity mechanisms imply pinned, mobile dislocations, in interaction with radiation-induced dispersed defect loop populations. This paper focuses on dislocation/loop interaction in including cross-slip mechanism, using 3D dislocation dynamics simulations. More specifically, we examined the representative “composite dislocation source” case, consisting of two connected arms or segments: one gliding in the primary slip plane, one gliding in the cross-slip plane. It is found that the cross-slipped segment fosters dislocation unpinning, no matter how strong the dislocation/loop interaction mechanism involved. In other words, the effective defect/loop interaction strength associated with the non-coplanar composite sources case is significantly lower than with the usual, coplanar dislocation source case. The present quantitative results indicate that cross-slip is possibly the dominant strain rate limiting mechanism, during post-irradiation plastic straining.

Keywords: composite screw dislocation source; radiation-induced defects; cross-slip segment; dislocation dynamics simulation

** Correspondence author
Email address: yang.li@cea.fr (Y. Li).

1. Introduction

Ferritic steels are widely used as structural nuclear materials, thereby subjected to radiation-induced degradations including hardening and embrittlement [1]-[4]. These detrimental evolutions are usually associated with the formation of dispersed defect cluster populations, in the form of sessile (immobile) dislocation loops [5]-[7]. Post-irradiation plastic strain takes the form of multiple wavy shear bands. Plastic strain spreading becomes more heterogeneous with increasing dose and can give rise to defect-depleted channels, where the defect/loops are progressively removed due to interactions with the mobile dislocations [8]-[11]. Channel-induced deformation can facilitate the initiation of brittle fracture and for this reason, is regarded as a crucial post-irradiation damage mechanism.

In this context, interactions with radiation-induced dispersed defect/loops eventually block/retard the initially mobile dislocations [12]-[14]. In principle, this means that relatively long dislocation arms are generated on both sides of the interacting (and fixed) defects, as the deformation proceeds. Such screw-type arms can then change their glide plane by cross-slip mechanism, thus providing an easy path across the dispersed defect populations [15]-[16]. Recent investigations of dislocation-loop interactions were carried out under periodic boundary conditions, using either atomistic Molecular Dynamics (MD) [17]-[19] or mesoscopic Dislocation Dynamics (DD) simulations [20]-[22]. Dislocations gliding in wavy shear bands however take the form of (relatively) short pinned dislocation segments. These dislocations (sources) are located at arbitrary positions, with respect to the interacting defects.

Understanding the actual shear band operation in post-irradiated steels thus requires analyzing dislocation source interaction with sessile loops, in presence of cross-slip mechanism. More specifically, our goal in this work is to explore the representative “composite dislocation” source case, in presence of different sessile loop types, using 3D dislocation dynamics simulations. A “composite dislocation” source involves two finite-length, connected screw segments: one gliding in the primary slip plane, one gliding in the cross-slip plane.

The following investigation approach is therefore adopted (see Section 2). Simulations using periodic boundary conditions (without pinning points) are carried out first, as a benchmarking, preliminary case (Section 3.1.1: $[1\bar{1}1]$ loop case; Section 3.2.1: $[111]$ loop case). The corresponding results allow validating the adopted simulation parameters and setup, by comparison with well-established MD simulation results. DD simulations of “composite dislocation” sources are conducted next and analyzed by comparison with the preliminary case results (Section 3.1.2: $[1\bar{1}1]$ loop case; Section 3.2.2: $[111]$ loop case).

2. Model and method descriptions

2.1 Dislocation Dynamics simulation setup and model: benchmarking case

All DD simulations results presented in this work are obtained using a 3D nodal code called NUMODIS (e.g. [21]-[23]), developed in CEA. The dislocation lines are described by a series of inter-connected nodes. Computation of the internal elastic stress and the

corresponding nodal force is carried out within the frame of the non-singular continuum elastic theory [24]. Nodal velocity is proportional to the effective resolved shear stress, as per:

$$v = \frac{\tau_{eff} b_s}{B_s} \quad (1)$$

where τ_{eff} is the effective resolved shear stress, b_s is the dislocation Burgers vector and B_s is a viscous coefficient whose value is function of the dislocation gliding systems ‘ s ’. All DD simulations herein are carried out at 300°K. The corresponding material parameters are listed in Table-1.

Viscous drag coefficient B_s (10^{-5} Pa s)	Burgers vector $b(10^{-10}$ m)	Shear modulus μ (GPa)	Poisson ratio ν
8	2.54	62.9	0.43

Tab. 1. Material parameters of Fe. The data comes from reference [21]

Our DD simulations are benchmarked by comparison with MD simulations using a similar configuration as shown in Fig. 1. The simulated crystal orientations as X, Y and Z axis are parallel to the $[\bar{1}\bar{1}2]$, $[1\bar{1}0]$ and $[111]$ directions, respectively. The DD simulated volume dimensions are: $L_X = 400$ nm, $L_Y = 300$ nm and $L_Z = 400$ nm, which is consistent with the shear bands thickness observed in post-irradiated materials [11],[25]. One screw dislocation source, with its Burgers vector \mathbf{b} parallel to the Z direction, is placed at the center of the

simulation volume. The total length of the source is L , which is comparable to the dimensions of the simulation volume.

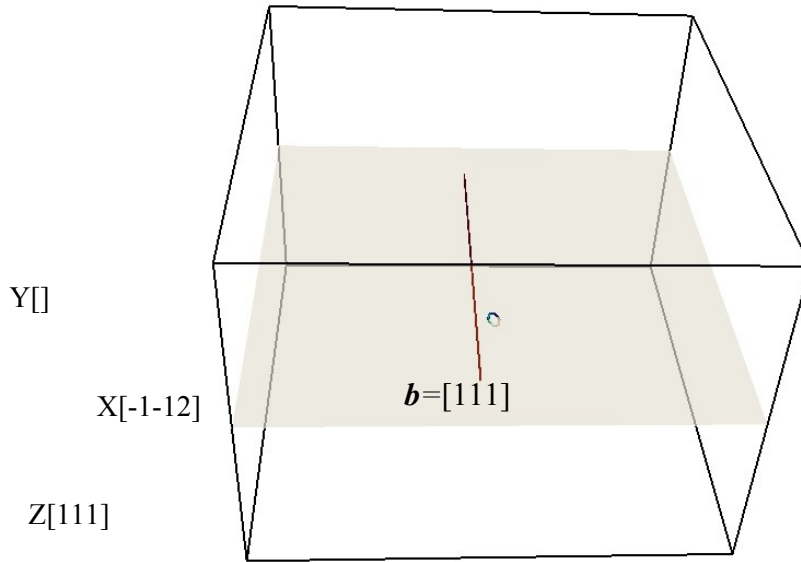


Fig. 1. DD simulation volume adapted to dislocation-loop interaction investigation. The highlighted primary slip plane contains a screw-type dislocation source. The dimension and interface properties are explained in the main text.

Simulation parameters and the corresponding slip systems of screw dislocations common to all the simulations are listed below:

Core-radius (Å)	Time step (ns)	Discretization	Primary slip	Cross-slip
		length (Å)	system	system
2.5	0.005	10	$(1\bar{1}0)[111]$	$(10\bar{1})[111]$

Tab. 2. Simulation parameters

One loop/obstacle is placed at a short distance from the mobile dislocation, as described in the next section.

2.2 Dislocation Dynamics simulation setup and model: dislocation source cases

A composite dislocation source configuration is shown in Fig. 2. The left-hand part of Fig. 2 defines the total source length L and source-loop initial standoff distances L_1 and L_2 . The implemented loop has a diameter D of 6 nm (typically found after 0.7 dpa at 300°C, in Fe [26]-[27]), placed at distance L_1 from segment BC. The center of the loop is coplanar with the dislocation line and L_2 from point B (at the center of segment BC). The chosen defect position (typically 15 nm or less) ensures early contact between the dislocation and the immobile defect/loop. Small variations of L_1 has a minor effect on the results since $L_1 \ll L$, while the influence of L_2 will be discussed in Section 3. The right-hand part of Fig. 2 shows the two segments AC and BC forming the composite source. Segment AC is L_{cs} long which glides in the cross-slip system and segment BC is L_p long and glides in the primary slip system.

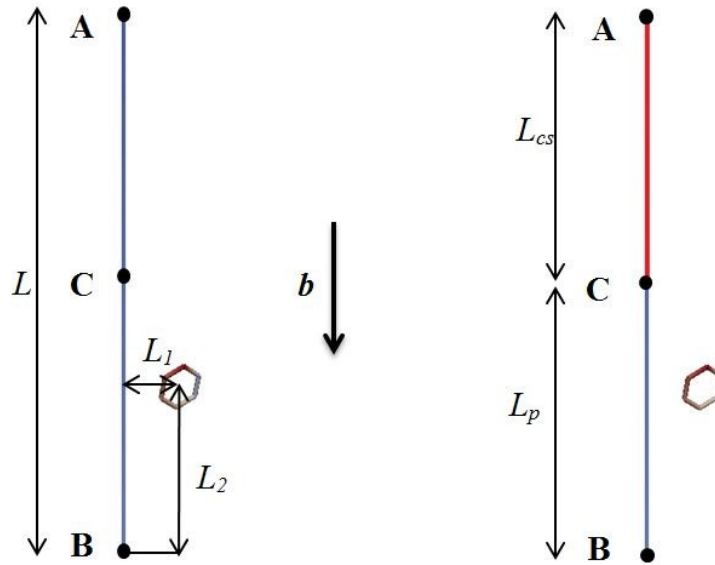


Fig. 2. Composite dislocation source configuration. Left-hand sketch: total source length L and definition of source-loop initial standoff distances L_1 and L_2 . Nodes A and B are fixed. Right-hand sketch: Segment AC is L_{cs} long and glides in the cross-slip plane $(10\bar{1})$; segment BC is L_p long and glides in the primary slip plane $(1\bar{1}0)$.

Nodes A and B are pinned, i.e. do not move during the simulation time similar to a Frank-Read source. Node C is the common point connecting the two segments gliding in different slip planes. For this reason, node C moves parallel to the initial direction of the dislocation line. If node C moves toward to node B, the length L_{cs} of segment AC increases and vice versa. It should be mentioned that the non-periodic boundary condition is used for all pinned configurations and the simulation is terminated whenever a dislocation node reaches one of the simulation volume boundaries.

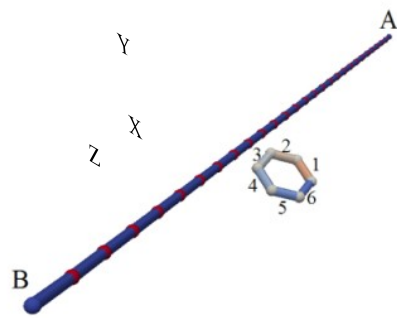
3. Results and discussion

3.1 Interaction with $[1\bar{1}1]$ loop

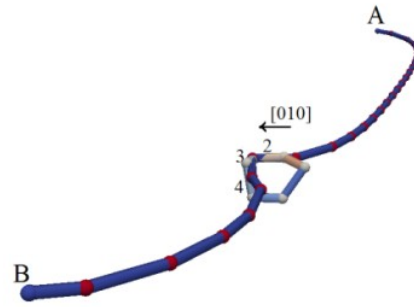
3.1.1 Interaction mechanism and obstacle strength: planar dislocation source

DD simulation results obtained using periodic boundary conditions are compared with MD simulation results. In this case, we used controlled of strain rate $\dot{\epsilon} = 10^6 \text{ s}^{-1}$ loading conditions (along Z direction). Interaction between the (coplanar) screw dislocation and the $[1\bar{1}1]$ loop changes the initial loop Burgers vector to $\mathbf{b} = [010]$, after the interaction is completed (not shown). The interaction strength corresponding to this mechanism is $\tau_c = 0.4\mu b/(L-D)$, in good agreement with corresponding MD results (i.e. $\tau_c = 0.38 \mu b/(L-D)$ from [17]).

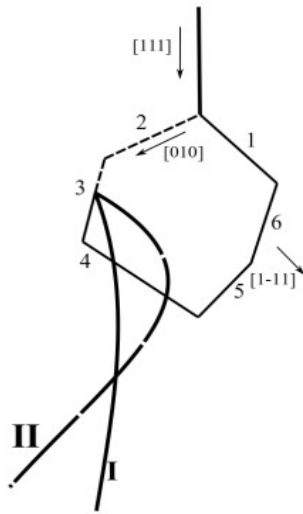
The next simulation case is carried out using exactly the same strain rate as before, this time using a finite-length dislocation source ($L = 300 \text{ nm}$), where nodes A and B are pinned (c.f. Fig. 2) and both segments AB and BC glide in the same primary slip plane $(1\bar{1}0)$. The resulting interaction mechanism is presented in Fig. 3. The screw dislocation is initially attracted by the loop and reacts with segment «2» (of the loop) to form a $[010]$ junction (Fig. 3(b)), according to Frank's rule ($1/2[111] - 1/2[1\bar{1}1] = [010]$). Thereafter, the new segments «3», «4» and the initial screw dislocation segments rearrange as shown in Figs. 3(c) (Case II) and 3(d). At this stage, the initial loop has two distinct parts, with Burgers vectors $\mathbf{b} = [1\bar{1}1]$ and $\mathbf{b} = [010]$. During the final interaction stage (Figs. 3(e), 3(f)), $\mathbf{b} = [010]$ of the junction segment returns to $\mathbf{b} = [1\bar{1}1]$.



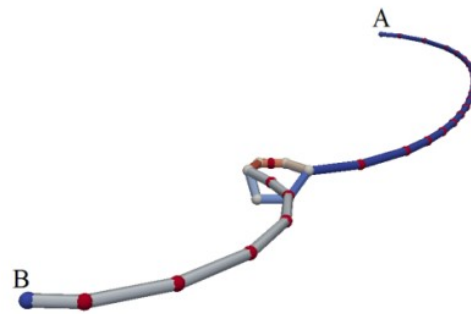
(a)



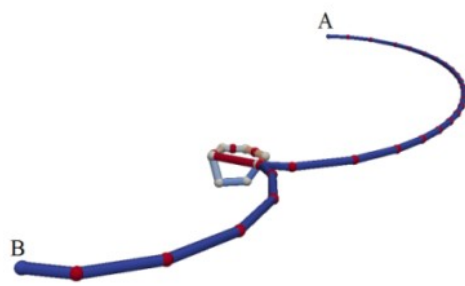
(b)



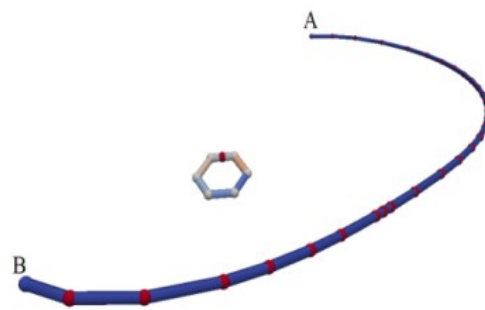
(c)



(d)



(e)



(f)

Fig. 3. Interaction between a coplanar, pinned screw dislocation and a $[1\bar{1}1]$ sessile loop. The screw dislocation glides in the direction of X-axis. The dislocation-loop interaction proceeds from frame (a) to frame (f). Frame (c) highlights the configurational difference achieved between the periodic boundary condition (Case I) and the composite source (Case II), shortly after the dislocation-loop contact time (corresponding to frame (b)).

Fig. 3(c) highlights the effect of using periodic boundary condition (Case I) on the dislocation-loop reaction. In Case I, the curvature radius of the interacting dislocation segment is maximal. At the time of contact, the incoming $b=[1\bar{1}1]$ screw arm can then easily adopt and keep its $\mathbf{b} = [010]$ orientation. The angle between the bowed-out dislocation segment and segment «3» is comparatively much larger (Case II). This condition lowers the attractive force between the incoming dislocation line and the remaining loop segments. The $\mathbf{b} = [010]$ junction segment cannot develop in this situation and usually collapses, after the interaction completion.

This configurational change also affects the effective loop interaction strength as shown in Fig. 4 for different source cases. The critical loop strength evolution corresponds to:

$$\tau_c = \tau_{eff} + \tau_{LT}^{extra} = \left(\alpha_{eff} + \frac{1}{\alpha_{LT}} \right) \frac{Gb}{L-D} \quad (2)$$

where G is the shear modulus (see Table-1), b is the Burgers vector modulus, $\alpha_{eff} = 0.4$ and $\alpha_c = 0.42$. The correction term α_c^{extra} represents the extra line tension contribution associated with the difference in local dislocation curvature (see Fig. 3(c)), due to the

pinning points of the finite length source [30]-[30]. It is important to note that the screw dislocation is systematically released before adopting a semi-circular bowed-out configuration, while the loop is mostly immobile (with respect to the dislocation). As a result, the line tension correction and the loop strength σ_c (~ 150 MPa) are nearly constant, regardless of L_2 (or L_p), within the $[L/6, L/2]$ range (see also Fig. 7 data, for different L_p and therefore, L_2 values).

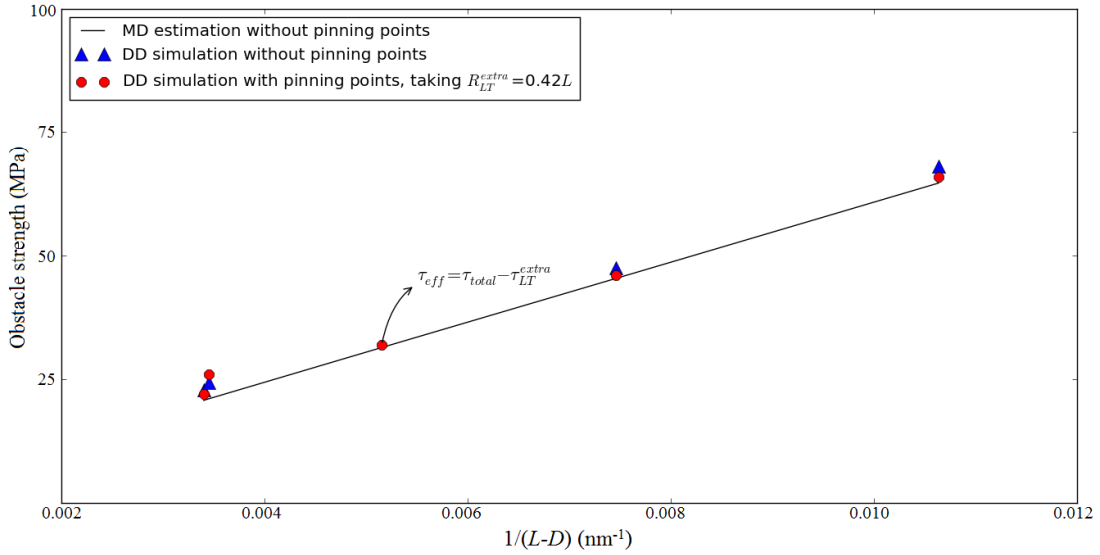


Fig. 4. $[1\bar{1}1]$ loop strength evolution with reciprocal source length $1/(L-D)$. In presence of periodic boundary conditions: DD simulation results closely match the MD simulations results. A finite length source includes pinning points, inducing dislocation curvature and hence, additional line tension stress σ_c^{extra} .

3.1.2 Interaction mechanism and effective obstacle strength: composite dislocation source

The composite dislocation source case is systematically investigated with four different simulation sets, using different constant applied stress (τ_p, τ_{cs}) conditions and finite L_{cs} long dislocation segments (see Table-3 and caption), gliding in the cross-slip plane.

	L (nm)	L_{cs} (nm)	$\tau_{p,min}$ (MPa)	$\tau_{p,max}$ (MPa)	$\tau_{p,inc}$ (MPa)	$\tau_{cs,min}$ (MPa)	$\tau_{cs,min}$ (MPa)	$\tau_{cs,inc}$ (MPa)
Set 1	300	50	100	200	20	100	200	20
Set 2	300	100	100	200	20	100	200	20
Set 3	300	150	100	200	20	100	200	20
Set 4	300	200	100	200	20	100	200	20

Tab. 3. Simulation sets including a composite dislocation source. Each set corresponds to several different simulations, where (τ_p, τ_{cs}) vary by $\tau_{p,inc}$ and $\tau_{cs,inc}$ steps of 20 MPa.

Each set is tested for different τ_{cs} levels acting on segment AC and varying from ($\tau_{cs,min} : \tau_{cs,max}$) and likewise, τ_p levels acting on segment BC varies from ($\tau_{cs,min} : \tau_{cs,max}$). Each simulation case is carried out up to a specific simulation time, t_{max} . The initial loading stress is set to 100 MPa, so segment AC (gliding in primary slip plane) contacts the obstacle at an early stage of each simulated case.

One typical dislocation-loop interaction case is presented in Fig. 5, for loading conditions $\tau_p = \tau_{cs} = 120$ MPa. Segment BC interacts with the obstacle in Fig. 5(b) and a $[010]$ junction is formed at the point of contact. Segment BC is then blocked since the resolved shear stress

τ_p is lower than the critical obstacle strength (from Fig. 4: $\sigma_c = \sigma_{total} = \sigma_{eff} + \dot{\epsilon}_c^{extra} \dot{\epsilon} \approx 150$ MPa). Meanwhile, segment AC propagates in the cross-slip plane and its length L_{cs} increases as node C moves along the line direction towards node B (Fig. 5(c)). As node C contacts with the loop/obstacle, a mutual attraction occurs between segments AC and BC then segment BC gets past the loop. Soon after, the whole dislocation source is transferred into the cross-slip plane (Fig. 5(d)). The loop is released at this time, while its Burgers vector returns to $[1\bar{1}1]$.

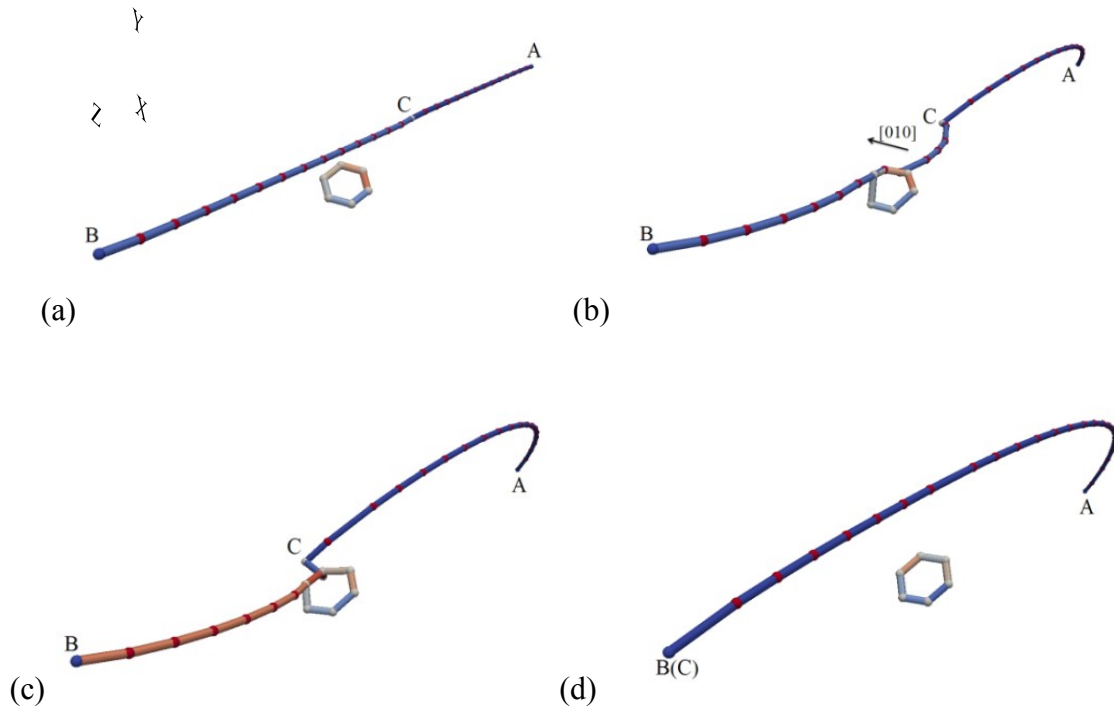


Fig. 5. Interaction between a composite dislocation source and a $[1\bar{1}1]$ loop. The source length $L_{cs} = 150$ nm for $\tau_p = \tau_{cs} = 120$ MPa. The mobile screw dislocation segment BC glides in the X direction. The dislocation-loop interaction proceeds from frame (a) through frame (d). Details regarding the interaction mechanism are provided in the main text.

The strain and node C position evolutions corresponding to Fig. 5 case are described in Fig. 6. During the early stages of the interaction, node C moves towards node B and hence, the cross-slip segment length L_{cs} gradually increases with time. After ~ 0.5 ns, segment BC is trapped by the loop and a plateau in the strain level was observed, accordingly. As segment AC continues to glide in the cross-slip plane, segment BC then starts changing its glide plane and node C resumes gliding toward the point B until $L = L_{cs}$. As node C meets with node B, the initial source is entirely transferred in the cross-slip plane, which generates a marked strain rate jump, after ~ 1 ns.

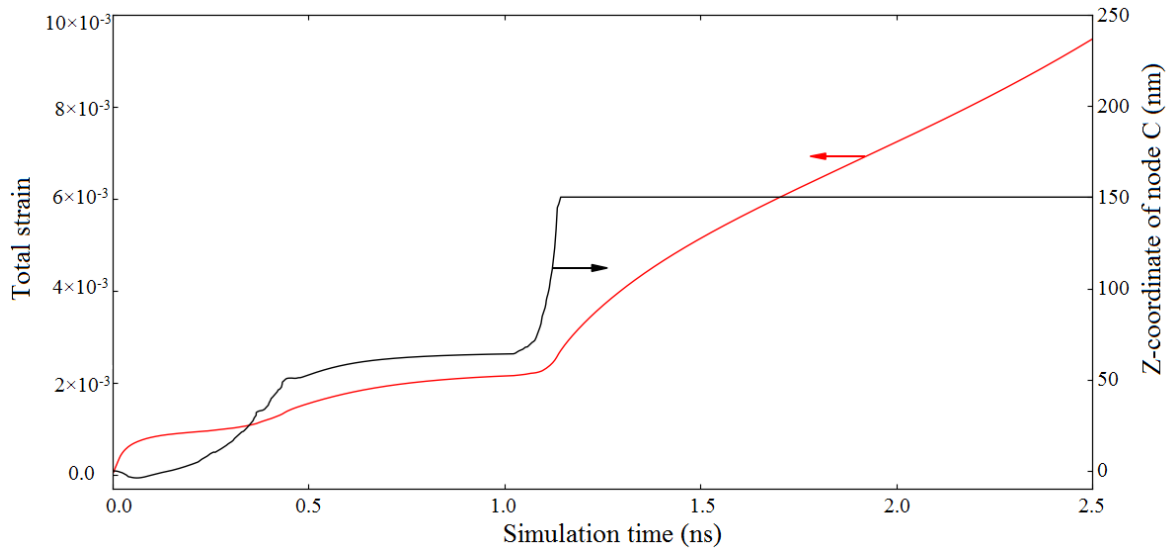


Fig. 6. The total strain and the corresponding node C position evolutions with the simulation time, for the $L_p = 150$ nm and $\tau_p = \tau_p = 120$ MPa case study. The initial position of node C corresponds to coordinate $Z = 0$.

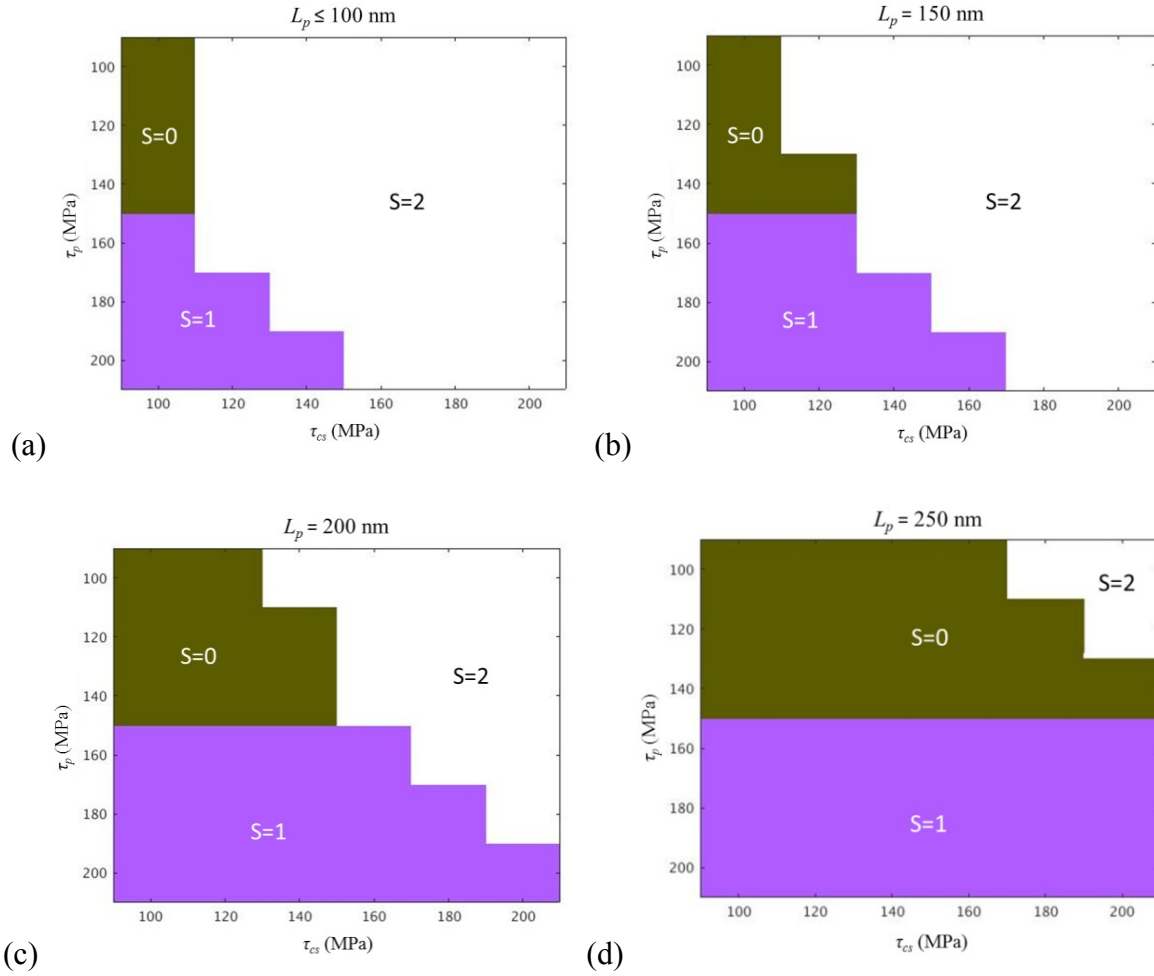


Fig. 7. Dislocation reaction case map corresponding to the constant applied stress conditions listed in Table-3. The x-axis refers to stress τ_{cs} acting on the cross-slip system and y-axis is the resolved stress τ_p acting on the primary slip plane. The 3 color codes are explained in the text. The results correspond to: (a) Set 4. (b) Set 3. (c) Set 2. (d) Set 1.

Simulation results associated with in Table-3 cases are presented in Fig. 7 in the form of triplet number series (τ_p, τ_{cs}, S) . The $S = 0$ (dark green) case indicates that the source is blocked by the obstacle; the $S = 1$ (purple) case indicates the source overcomes the defect

while gliding in the primary slip plane; the $S = 2$ (white) case indicates the source overcomes the defect while gliding in the cross-slip plane (as in Fig. 5). Fig. 7 shows that a screw dislocation can directly cut through the obstacle provided $\tau_p > 150$ MPa which is consistent with Fig. 4 results. Obstacle by-passing occurs if $\tau_{cs} > \tau_{critical}(L_p)$ and $\tau_{cs} \geq \tau_p$ where $\tau_{critical}(L_p) = 120$ MPa if $L_p = 150$ nm; while $L_p > 150$ nm induces higher $\tau_{critical}(L_p)$. It should be noted that $\tau_{critical}(L_p = 150 \text{ nm})$ is lower than $\tau_{critical}(L_p = 300 \text{ nm})$ in absence of cross-slipped segment AC, i.e. 120 MPa instead of 150 MPa.

The strain evolutions corresponding to different $L_{cs} = L_p = 150$ nm cases are shown in Fig. 8. Fig. 8(a) presents the time evolution of the total strain rate for $\tau_p = 120$ MPa, for different τ_{cs} values ranging from 100 MPa to 180 MPa (Fig. 8(a), curves B, C, D). These results are compared with the strain rate evolution of coplanar source case, using $L_p = 300$ nm (Fig. 8(a), curve A). The cross-slipping time and the post-interaction strain rate strongly depend on the τ_{cs} level.

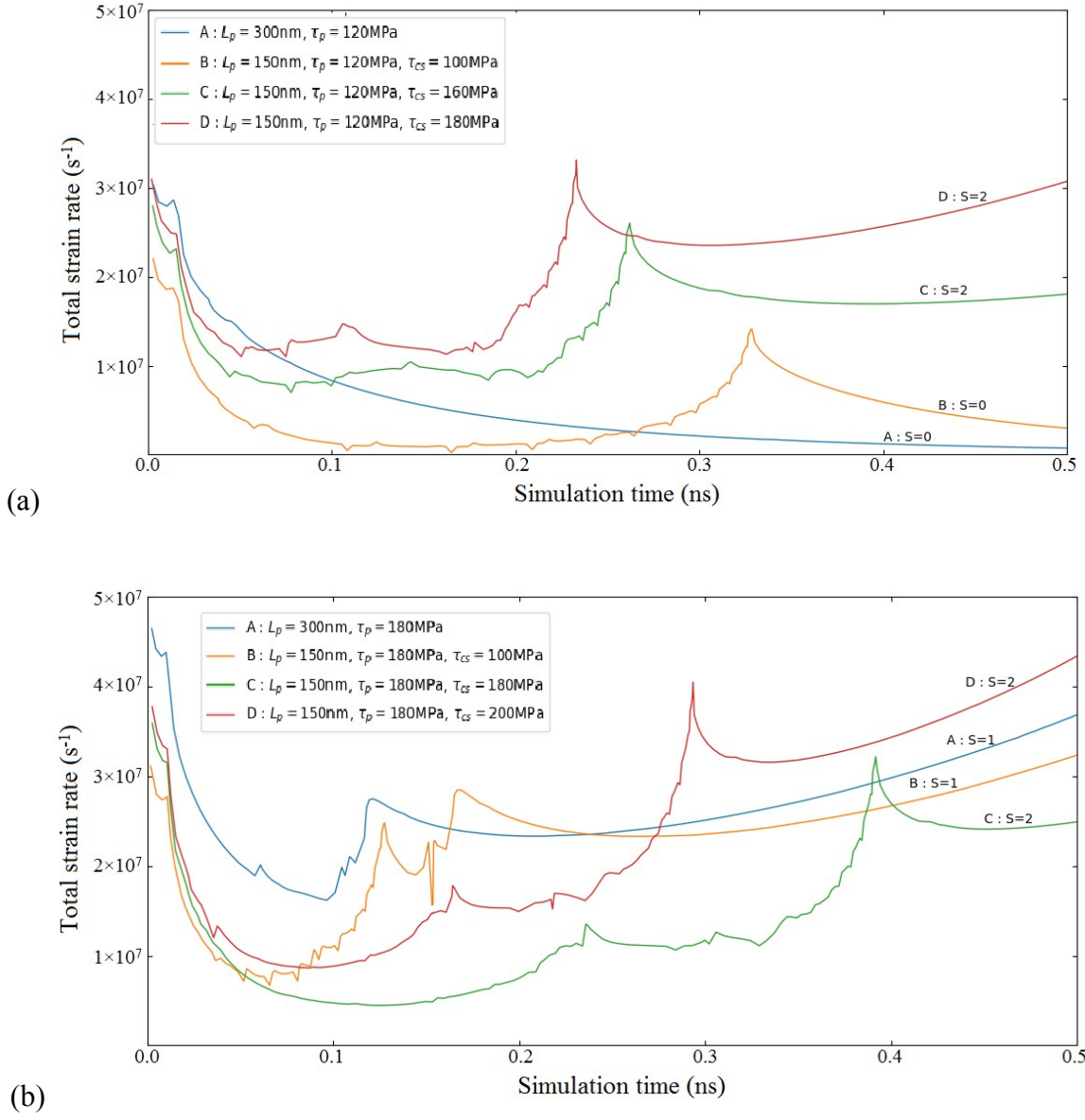


Fig. 8. Total strain rate evolutions versus time associated with simulation setup 3 ($L_{cs} = L_p = 150$ nm), for different loading combinations (τ_p , τ_{cs}). (a) $\tau_p = 120$ MPa and τ_{cs} varies from 100 to 180 MPa. (b) $\tau_p = 180$ MPa and τ_{cs} varies from 100 to 200 MPa. The different curves A, B, C, D are further described in the main text.

In Fig. 8(b) cases ($\tau_p = 180$ MPa), no dislocation source blocking (strain rate = 0) is observed (see Fig. 8(a), curve A, for example). In addition, node C reaches node A for a significantly smaller τ_{cs} level, as compared to $\tau_p = 120$ MPa cases in Fig. 8(a). If $\tau_{cs} < 160$ MPa (Fig. 8(b) curve B), segment BC directly cuts through the obstacle, generating a sharp strain rate jump at $t = 0.12$ ns. The second peak appears as the source is entirely transferred into the primary slip plane. In the $L_p = 300$ nm case (Fig. 8(b) curve A), the dislocation velocity is faster due to the lack of the competition between segments AC and BC. Similarly, in $\tau_{cs} > \tau_p$ case (Fig. 8(b), curve D), loop by-passing mechanism occurs with a slower strain evolution. The presence of the cross-slipped segment AC (for the case of $L_{cs} > 1/3L$) systematically helps the primary segment BC to get past the obstacle, including for τ_p and τ_{cs} levels below the critical obstacle strength τ_c (from Fig. 4: $\tau_c \approx 150$ MPa). This effect reduces with the decrease of the cross-slip segment length L_{cs} .

In order to evaluate the separate contribution of cross-slip on the dislocation-loop interaction strength, we finally replaced the $[1\bar{1}1]$ loop with a hard, impenetrable platelet (or facet). The facet position, size and orientation are exactly the same as those of the $[1\bar{1}1]$ loop. The studied case corresponds to $L_p = 150$ nm with $\tau_p = \tau_{cs} = 120$ MPa. The reader should note that the implemented facet does not generate any long-range stress. The total strain and the corresponding strain rate evolutions versus the simulation time are shown in Fig. 9. In the loop case, the entire dislocation-loop interaction time is ~ 1 ns. The total reaction time is nearly the same in the facet case (~ 10 ps shift), with a relative total strain error of about 1.78%, at the reaction completion time. This demonstrates that the strain rate

achieved during interaction with a $[1\bar{1}1]$ loop is mainly controlled by the cross-slip mechanism. The reaction map (not shown) corresponding to the hard facet case is exactly the same as that of the loop case (c.f. Fig. 6).

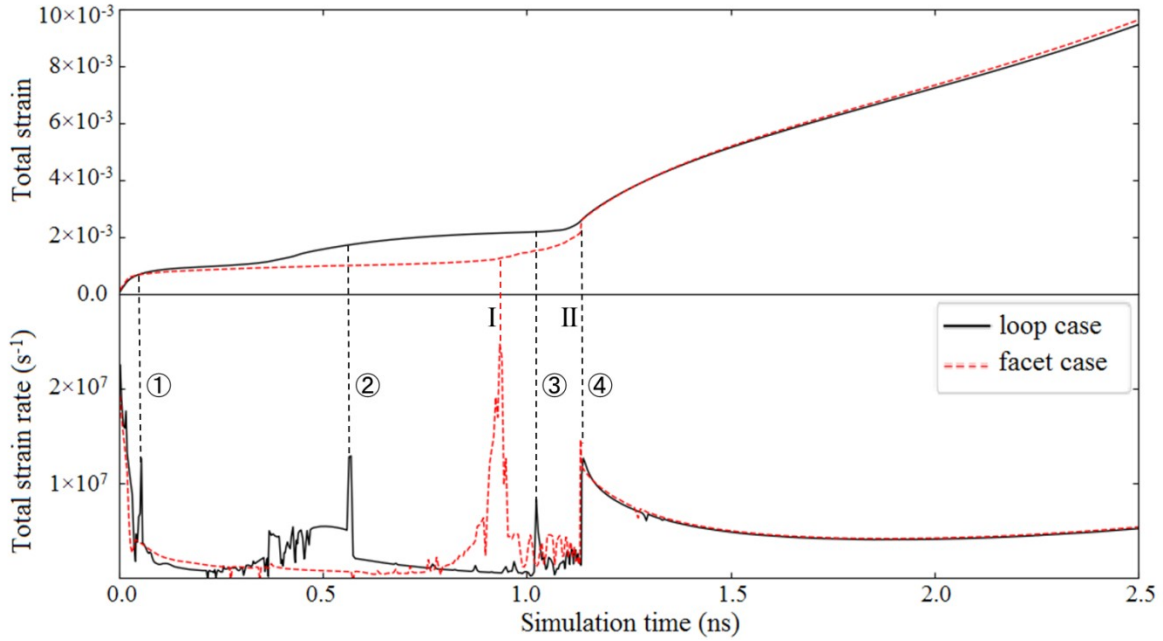


Fig. 9. Time evolutions of the total strain (upper frame) and corresponding strain rate (lower frame) during dislocation-defect interaction. The mobile segment length is $L_p = 150$ nm and $\tau_p = \tau_{cs} = 120$ MPa. The loop and facet cases are denoted by solid and dashed lines, respectively. In the loop case, the junction is formed in ①, where the mobile dislocation segment is attracted by the loop; in ②: the common node C reaches the loop; in ③: the dislocation segment is totally released by the loop; in ④: the dislocation is entirely transferred towards the cross-slip plane. For the facet case, in I: the dislocation segment bypasses the facet; in II: the dislocation is entirely transferred in the cross-slip plane. The

small fluctuations taking place between I and II (or ③ and ④) are due to the discrete description of the dislocation segments (node insertion or removal).

3.2 Interaction with $[111]$ loop

3.2.1 Interaction mechanism and obstacle strength: coplanar dislocation source

The screw dislocation and periodic boundary condition case is first examined, using fixed strain rate conditions as in section 3.1.1. In this case, the sessile loop is absorbed in the form of a helical turn [18] which then closes itself and leaves a $[111]$ loop behind, as the screw dislocation breaks away. This mechanism is associated with a critical interaction stress $\tau_c = 0.72\mu b/(L-D)$ in agreement with [18].

The coplanar finite-length (pinned) dislocation source case is examined next (see Fig. 10). A helical turn is formed during the first stages of the interaction (Fig. 10(b)), then after a significant bow-out of the dislocation, the helical turn reconnects and re-emits the initial loop in a process similar to Hirsch's mechanism [30] (Fig. 10(e)). This configuration induces higher obstacle strength as compared to the $[1\bar{1}1]$ loop case, owing to the larger line tension buildup. The corresponding critical interaction stress $\tau_c = 240$ MPa could be obtained from the Eq. (2) taking $\alpha_{eff} = 0.72$ and $\alpha_i = 0.25$. It is interesting to note that the helical turns move together with the bowed-out dislocation (Figs. 10(c) and 10(d)). As a result, the obstacle strength depends on the initial position L_2 (see Fig. 2). If $L_2 = L/2$ for example, the obstacle strength $\tau_c \approx (\alpha_{eff} + 1/\alpha_i) \mu b/(L-D)$ for $\alpha_i = 0.48$ instead of 0.25. This means the $[111]$ loop is released before the dislocation bow-out adopts a semi-circular

configuration. Only $L_p = L_{cs} = 150\text{nm}$ case is presented hereafter, for simplicity. Different applied stress conditions (τ_p, τ_{cs}) are examined in the next section, for the composite dislocation source case study.

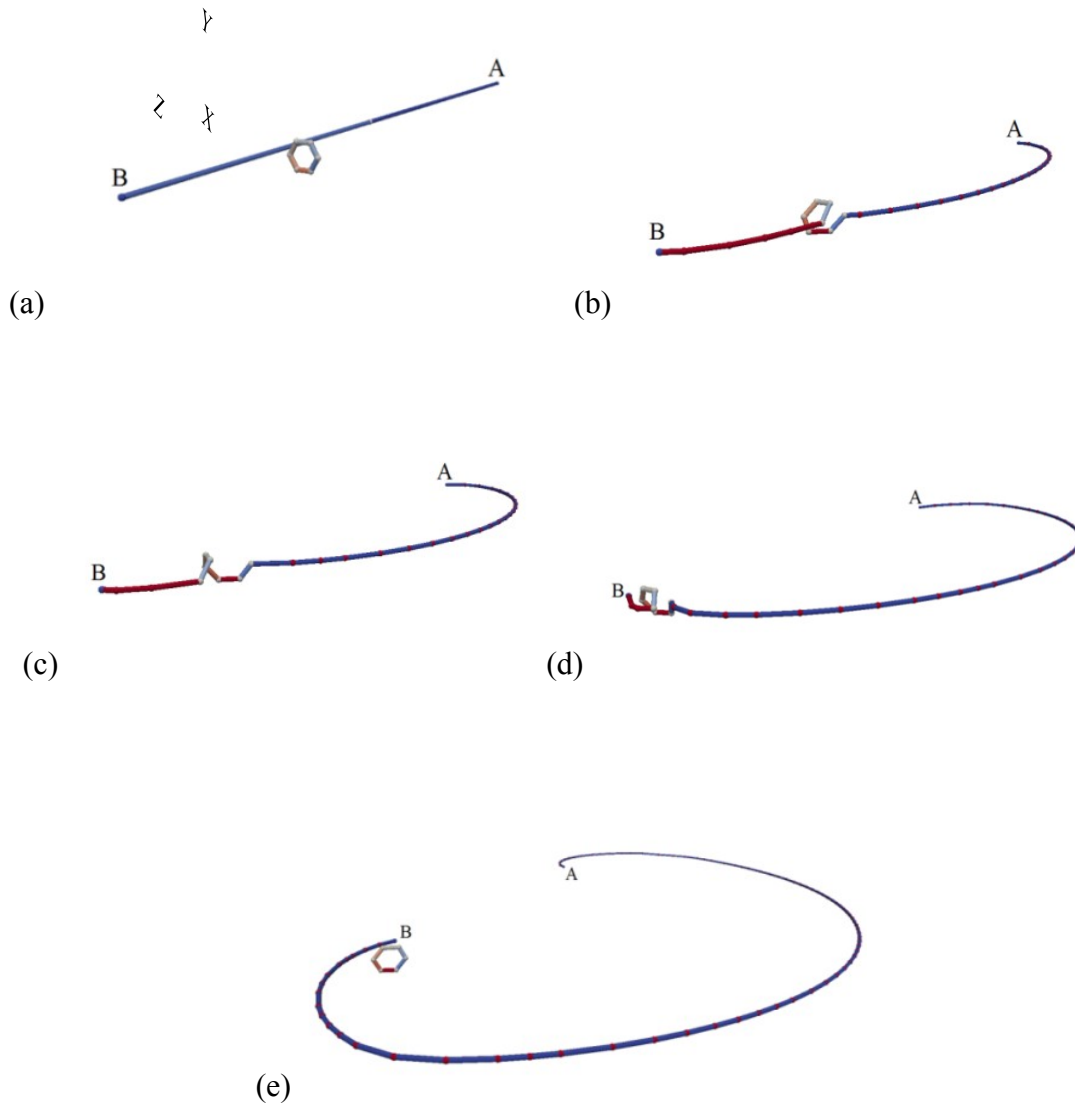


Fig. 10. Interaction between a coplanar pinned dislocation source and a $[111]$ loop. The (screw-type) dislocation source glides in the X direction. A helical turn is formed in frame (b), which subsequently propagates towards point B, while AB segments glides and bows-

out. The helical turn is released in frame (e). The interaction results in the net displacement of the initial loop, which is reformed near the pinning point B. the source length $L = 300$ nm.

3.2.2 Interaction mechanism and obstacle strength: composite dislocation source

The results associated with $L_{cs} = 150$ nm case are presented in Fig. 11. In Fig. 11(a), the critical stress range is comprised between 130 MPa and 280 MPa, in consistence with the helical turn mechanism strength. A fourth interaction mechanism is introduced in Fig. 11(a) (S=3, black color area), where the dislocation bow-out keeps gliding without the helical turn closure. In this case, neither AC nor BC segment can overrun the other. The helical turn is then simply dragged away, since the loop and the incoming screw share the same Burgers vector. Similarly, interaction strength of the composite source is lower than that in the coplanar source case, under comparable loading conditions (see also Fig. 11(b)).

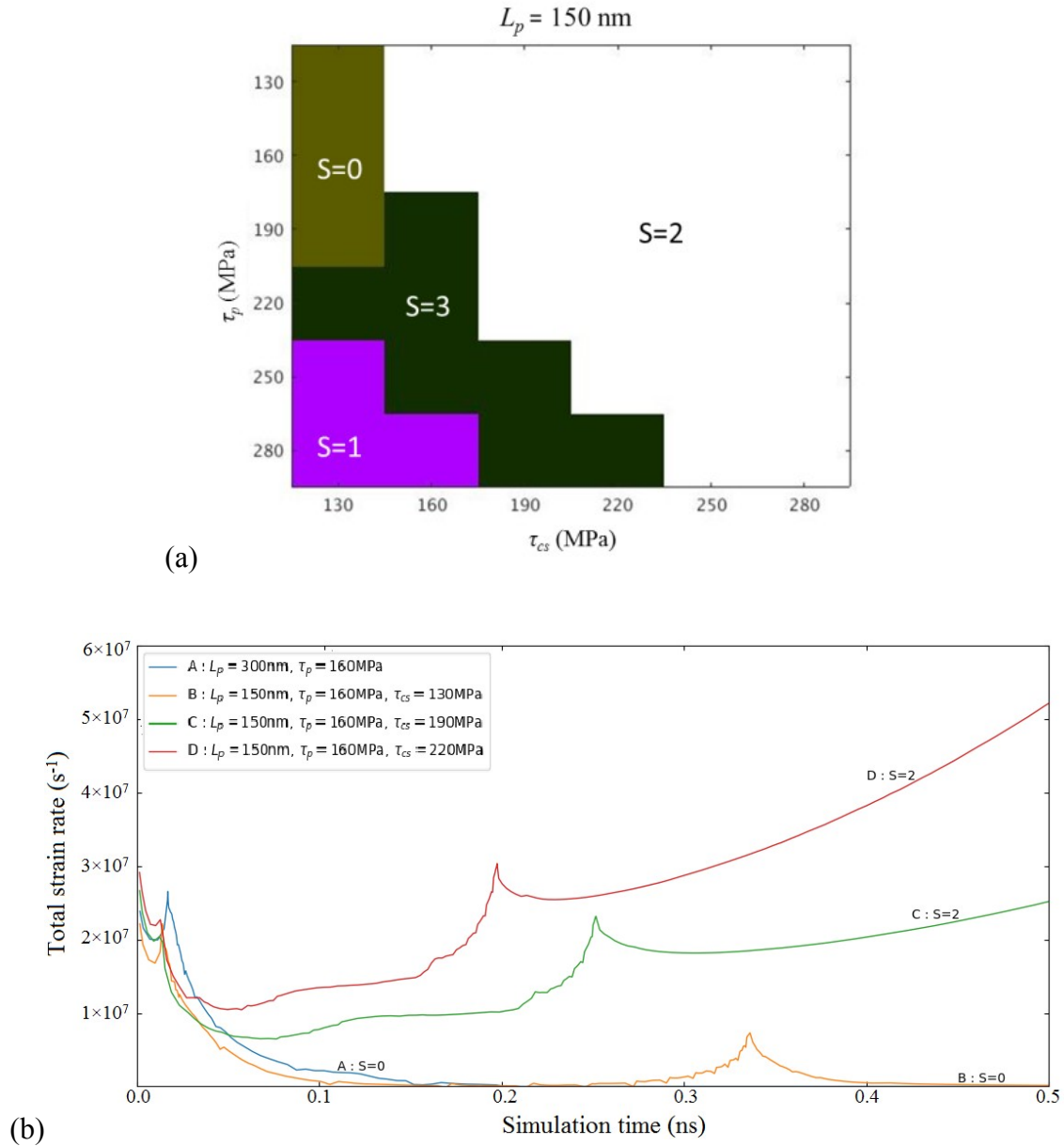


Fig. 11. Composite source interaction ($L_{cs} = 150\text{nm}$) with a $[111]$ loop. (a) The different interaction mechanisms are indicated by different color, depending on the considered applied stress (τ_p , τ_{cs}) combination. Mechanisms $S = 0, 1, 2, 3$ are explained in the main text. (b) Total strain rate evolutions versus time for $\tau_p = 160 \text{ MPa}$ and τ_{cs} varying from 130

to 220 MPa. The interaction mechanism, the cross-slipping time and the post-interaction total strain rate strongly depends on the τ_{cs} level.

Lastly, a simulation case where the $[111]$ loop is replaced by a $[\bar{1}11]$ oriented hard facet (not shown) is carried out. It is recalled that unlike the loop, the facet has no associated stress field; whereas interaction with a facet involves none of the dislocation recombination mechanisms associated with loop interaction. In this way, we found that interaction with the facet is similar to interaction with a $[\bar{1}11]$ loop, as presented in Section 3.1.2. This comparison further confirms that, in presence of cross-slip, the effective loop/obstacle interaction strength weakly depends on the loop-induced elastic stress field or the particular dislocation-loop interaction mechanism.

4. Conclusions

Interaction between screw-type dislocation sources with $[\bar{1}11]$ and $[111]$ loops is investigated using 3D nodal dislocation dynamics simulations. The comparative interaction strength levels associated with $[\bar{1}11]$ and $[111]$ loops are evaluated using co-planar source cases first, where all the initial source segments glide in the same primary slip plane. Coplanar sources are used: I) infinitely long dislocation segments, due to the periodic boundary conditions, II) in the form of a finite-length, pinned dislocation segments. Case-I is adopted as a benchmarking case, for validating our DD simulation model and setup by comparison with well-established MD simulations results.

1. Interaction strength associated with $[1\bar{1}1]$ or $[111]$ loop is significantly larger in finite-length source case (case-II) than in periodic boundary conditions case (case-I). Pinned source nodes induce a local dislocation curvature and associated extra line tension contribution, adding up to the total effective interaction strength.

The case of composite dislocation sources is further investigated. This configuration includes two distinct (L_p, L_{cs}) long segments, gliding in the primary and cross-slip planes, respectively. The effect of various loading conditions (τ_p, τ_{cs}) on the effective interaction strength is examined, in terms of interaction mechanisms and time evolution of the strain rate.

2. The presence of a cross-slipped segment L_{cs} could systematically reduce the resolved shear stress needed to unpin the screw dislocation if $L_{cs} > 1/3L$. The interaction strength level directly depends on the cross-slip segment length L_{cs} .
3. The cross-slip effect is dominant regardless of the particular loop type involved ($[1\bar{1}1]$ or $[111]$), i.e. regardless of the particular loop-induced interaction mechanism and loop-induced stress field.

In conclusion, the results indicate that cross-slip is possibly the dominant strain rate limiting mechanism, in presence of disperse loop populations.

Acknowledgements

This work has been carried out within the framework of the EUROfusion Consortium and has received funding from the Euratom research and training programme 2014-2018 under grant agreement No 633053. The views and opinions expressed herein do not necessarily reflect those of the European Commission. The complementary support of the Materials Research Program RMATE of the Nuclear Energy Division of the French Atomic Energy Commission (CEA/DEN) is also acknowledged.

References

- [1] E.E. Bloom, The challenge of developing structural materials for fusion power systems, *J. Nucl. Mater.* 258 (1998) 7-17.
- [2] M. Matijasevic, E. Lucon, A. Almazouzi, Behavior of ferritic/martensitic steels after n-irradiation at 200 and 300°C, *J. Nucl. Mater.* 377 (2008) 101-108.
- [3] N. Baluc et al., Status of reduced activation ferritic/martensitic steel development, *J. Nucl. Mater.* 367 (2007) 33-41.
- [4] M. Matijasevic, W. Van Renterghem, A. Almazouzi, Characterization of irradiated single crystals of Fe and Fe-15Cr, *Acta Mater.* 57 (2009) 1577-1585.
- [5] Y.A. Nikolaev, A.V. Nikolaeva and Y.I. Shtrombakh, Radiation embrittlement of low-alloy steels, *Int. J. Pres. Ves. Pip.* 79 (2002) 619-636.
- [6] R.L. Klueh et al., Embrittlement of reduced-activation ferritic/martensitic steels irradiated in HFIR at 300 °C and 400 °C, *J. Nucl. Mater.* 283 (2000) 478-482.
- [7] M. Victorian, N. Baluc et al., The microstructure and associated tensile properties of irradiated fcc and bcc metals, *J. Nucl. Mater.* 276 (2000) 114-122.
- [8] Q. Wei et al., Evolution and microstructure of shear bands in nanostructured Fe, *Appl. Phys. Lett.* 81 (2002) 1240-1242.
- [9] T.S. Byun, E. H. Lee, and J. D. Hunn, Plastic deformation in 316LN stainless steel—characterization of deformation microstructures, *J. Nucl. Mater.* 321 (2003) 29-39.
- [10] T.S. Byun, N. Hashimoto, and K. Farrell, Temperature dependence of strain hardening and plastic instability behaviors in austenitic stainless steels, *Acta Mater.* 52 (2004) 3889-3899.
- [11] G.R. Odette et al., Modeling the multiscale mechanics of flow localization-ductility loss in irradiation damaged bcc alloys, *J. Nucl. Mater.* 307 (2002) 171-178.

- [12] S.J. Zinkle and Y. Matsukawa, Observation and analysis of defect cluster production and interactions with dislocations, *J. Nucl. Mater.* 329 (2004) 88-96.
- [13] J.S. Robach et al, In-situ transmission electron microscopy observations and molecular dynamics simulations of dislocation-defect interactions in ion-irradiated copper, *Philo. Mag.* 83 (2003) 955-967.
- [14] M. Victoria et al., The microstructure and associated tensile properties of irradiated fcc and bcc metals, *J. Nucl. Mater.* 276 (2000) 114-122.
- [15] A. Kelly and R.B. Nicholson, *Strengthening method in crystals*, First ed., Elsevier, New York, 1971, p. 156.
- [16] C.S. Shin, M.C. Fivel et al., Dislocation-impenetrable precipitate interaction: a three-dimensional discrete dislocation dynamics analysis, *Philo. Mag.* 83 (2010) 3691-3704.
- [17] X.Y. Liu and S.B. Biner, Molecular dynamics simulations of the interactions between screw dislocations and self-interstitial clusters in body-centered cubic Fe, *Scripta Mater.* 59 (2008) 51-54.
- [18] D. Terentyev, D.J. Bacon and Yu.N. Osetsk, Reactions between a $\frac{1}{2}$ $\langle 111 \rangle$ screw dislocation and $\langle 100 \rangle$ interstitial dislocation loops in alpha-iron modelled at atomic scale, *Philo. Mag.* 90 (2009) 1019-1033.
- [19] D. Terentyev et al., Simulation of the interaction between an edge dislocation and a $\langle 100 \rangle$ interstitial dislocation loop in α -iron, *Acta Mater.* 56 (2008) 5034.
- [20] J.R. Greer, C.R. Weinberger, W. Cai, Comparing the strength of fcc and bcc sub-micrometer pillars: Compression experiments and dislocation dynamics simulations, *Mater. Sci. Eng. A*, 493 (2008) 21-25.
- [21] S.J. Shi et al., Interaction of $\langle 100 \rangle$ dislocation loops with dislocations studied by dislocation dynamics in α -iron, *J. Nucl. Mater.* 460 (2015) 37-43.
- [22] J. Drouet, L. Dupuy et al., Dislocation dynamics simulations of interactions between gliding dislocations and radiation induced prismatic loops in zirconium, *J. Nucl. Mater.* 449 (2014) 252-262.

- [23] J. Drouet, L. Dupuy et al., A direct comparison between in-situ transmission electron microscopy observations and Dislocation Dynamics simulations of interaction between dislocation and irradiation induced loop in a zirconium alloy, *Scripta Mater.* 119 (2016) 71-75.
- [24] W. Cai et al., A non-singular continuum theory of dislocations, *Mech. Phys. Solids* 54 (2006) 561-587.
- [25] K. Gururaj, C. Robertson and M. Fivel, Channel formation and multiplication in irradiated FCC metals: a 3D dislocation dynamics investigation, *Philo. Mag.* 95 (2015) 1368-1389.
- [26] M. Matijasevic, E. Lucon, A. Almazouzi, Behavior of ferritic/martensitic steels after n-irradiation at 200 and 300°C, *J. Nucl. Mater.* 377 (2008) 101-108.
- [27] L.L. Horton, J. Bentley and K. Farrel, A TEM study of neutron-irradiated iron, *J. Nucl. Mater.* 108 (1982) 222-233.
- [28] A.J.E. Foreman, The bowing of a dislocation segment, *Philo. Mag.* 15 (137) 1011-1021.
- [29] D. Hull and D.J. Bacon, *Introduction to dislocations*, Fourth Ed., Elsevier, Butterworth-Heinemann, 2001.
- [30] P.B. Hirsch, In *Vacancies' 76*. Proceedings of a conference on 'point defect behavior and diffusional processes' organized by the Metals Society and held at The Royal Fort, University of Bristol, on 13-16 September, 1976.